Ideal ballooning modes in the tokamak scrape-off layer

Federico D. Halpern, Sebastien Jolliet, Joaquim Loizu, Annamaria Mosetto, and Paolo Ricci

Additional information on Phys. Plasmas

Ideal ballooning modes in the tokamak scrape-off layer

Federico D. Halpern,[a)] Sebastien Jolliet, Joaquim Loizu, Annamaria Mosetto,
and Paolo Ricci
*École Polytechnique Fédérale de Lausanne (EPFL), Centre de Recherches en Physique des Plasmas,
Association Euratom-Confédération Suisse, CH-1015 Lausanne, Switzerland*

A drift-reduced Braginskii fluid model is used to carry out a linear and non-linear study of ideal ballooning modes in the tokamak scrape-off layer. First, it is shown that the scrape-off layer finite connection length and boundary conditions modify the ideal stability limit with respect to the closed flux-surface result. Then, in a two-fluid description, it is found that magnetic induction effects can destabilize long wavelength resistive ballooning modes below marginal ideal stability. Non-linear simulations confirm a gradual transition from small scale quasi-electrostatic interchange turbulence to longer wavelength modes as the plasma beta is increased. The transition to global ideal ballooning modes occurs, roughly, at the linearly obtained stability threshold. The transport levels and the pressure gradient as a function of plasma beta obtained in non-linear simulations can be predicted using the non-linear flattening of the pressure profile from the linear modes as a turbulent saturation mechanism. [http://dx.doi.org/10.1063/1.4807333]

I. INTRODUCTION

Ideal magnetohydrodynamic (MHD) phenomena have been known to limit the maximum achievable β in tokamak plasmas since the 1980s[1] ($\beta = 2\mu_0 p/B^2$ is the ratio of plasma kinetic to magnetic pressure). Ideal ballooning instabilities, in particular, can limit the maximum achievable pressure gradient at any plasma magnetic surface.

The main features of ideal ballooning modes were described in the late 1970s and early 1980s.[2–4] They are flute-like modes that become unstable when pressure perturbations driven by bad curvature cannot be compensated by parallel spreading due to the shear Alfvén wave. A simple stability criterion for this instability can be derived by balancing the pressure drive $\sim\nabla p$ against the field line bending term $\sim\nabla_\parallel j_\parallel$. The result is that ideal ballooning modes become unstable when the ideal ballooning stability parameter α exceeds a critical pressure gradient, $\alpha = q^2\beta_e R/L_p \gtrsim \alpha_{\rm crit} \sim 1$ (the tokamak safety factor is approximated as $q = rB_\phi/(RB_\theta)$ in the cylindrical limit; $\beta_e = 2\mu_0 p_e/B^2$ is the electron beta; and $L_p = -p/\nabla p$ is the pressure gradient length). The effects of good and bad curvature, magnetic shear, shaping, and diamagnetic flows can significantly modify the stability threshold.[2–6]

While electromagnetic effects and the onset of the ideal ballooning mode have been addressed with numerical simulations using core (see, e.g., Refs. 1 and 7) and edge (see, e.g., Refs. 8 and 9) relevant geometry and parameters, such study has not been carried out for the scrape-off layer. The objective of this work is to specifically address the properties of ideal ballooning modes in this region. In particular, we would like to address the following questions: what are the stability threshold, the growth rate, and the non-linear turbulent dynamics of ideal ballooning modes in the tokamak scrape-off layer?

These issues are particularly important since the phase space of tokamak operation shows an inaccessible regime that can be reached as β is increased in the scrape-off layer at high collisionality.[10,11] This inaccessible parameter space region has been interpreted as the "density limit" and, up to now, it has been studied using simulations based on edge-relevant configurations. By using three-dimensional electromagnetic edge turbulence simulations, Rogers and Drake proposed that the density limit results from enhanced transport due to electromagnetic effects:[8,12] electromagnetic flutter inhibits the growth of the sheared flows responsible for saturation of resistive ballooning modes and, in turn, this leads to the onset of catastrophic transport. A β scaling in edge transport, due to a modification of electron parallel dynamics through magnetic induction, was found by Scott using a gyrofluid model[13] and later by Naulin[14] using a fluid model. In more recent gyrofluid simulations of edge turbulence,[9] heat and particle transport are significantly enhanced above a critical pressure gradient $\alpha_{\rm crit} \sim 0.2 - 0.6$ with $\hat{s} = 1$, which is significantly lower than the classical result $\alpha_{\rm crit} \approx 0.8$. (Here $\hat{s} = rq'/q$ is the magnetic shear.) In Ref. 9, it is argued that ideal ballooning modes become unstable below their linear threshold because of the existence of a non-linear drive.

Scrape-off layer plasmas are cold and collisionality plays an important role. The dominant turbulent modes have low frequency and small perpendicular wave number. Therefore, a fluid or gyrofluid treatment is typically used. As a matter of fact, the key characteristics of the scrape-off layer turbulent phase space appear to be captured by the electromagnetic fluid drift turbulence theory (see, for example, Refs. 8, 15–21).

In order to address the stability and turbulent dynamics of ideal ballooning modes in the scrape-off layer, we use a global, drift-reduced Braginskii fluid model[22] in combination with a proper set of boundary conditions at the magnetic pre-sheath entrance.[23] We carry out flux-driven, global 3D

a)Electronic mail: federico.halpern@epfl.ch

simulations in $\hat{s} - \alpha$ geometry with a toroidal limiter on the equatorial plane at the high-field side. This configuration can capture the principal elements of scrape-off layer turbulence: flute-like fluctuations with amplitude comparable to the background quantities; lack of scale-length separation between fluctuations and background; and parallel losses to the limiter that are determined by sheath physics. Moreover, thanks to the relative simplicity of the setup, we develop a better understanding of the underlying phenomena by using the analytical theory and linear calculations whenever possible.

Our main findings can be summarized as follows. First, linear ideal MHD calculations indicate that the scrape-off layer finite connection length and boundary conditions modify the ideal stability limit. In particular, the vanishing of the electrostatic potential perturbation at the limiter must be captured correctly; otherwise, the linear threshold of the ideal ballooning mode can be underestimated. Second, using a linear drift-reduced Braginskii model, it is found that magnetic induction effects can destabilize long wavelength resistive ballooning modes well below the marginal ideal stability limit. Third, the aforementioned effects found from the linear theory have been recovered in fully 3D non-linear simulations using the drift-reduced Braginskii model. In particular, the non-linear simulations confirm a gradual transition from quasi-electrostatic interchange turbulence to global ideal ballooning modes. The appearance of the global modes roughly takes place at the linear ideal ballooning stability limit. In the ideal unstable regime, we observe global modes with the longest poloidal and toroidal wavelengths allowed by the system. Finally, we have used the linear theory together with a non-linear turbulent saturation rule[24,25] to predict the scaling of the pressure profile length as a function of β; the results of the calculation are in good agreement with the non-linear dynamics observed in the simulations.

This paper is organized as follows. After introducing our model (Sec. II), we address the linear stability of ideal ballooning modes in open field lines within the ideal (Sec. IV) and two-fluid (Sec. IV) models. Then, non-linear two-fluid simulation results demonstrating the ideal ballooning stability limit are described in Sec. V. The results can be interpreted by combining our linear understanding of scrape-off layer stability with a non-linear turbulent saturation rule (Sec. VI). The findings of the study are summarized in Sec. VII.

II. DRIFT REDUCED BRAGINSKII EQUATIONS AND BOUNDARY CONDITIONS

Here, we briefly recall the two-fluid model that is used to study scrape-off layer stability and transport. The model is described fully in Ref. 22. The use of a fluid model is justified by that fact that, in the tokamak scrape-off layer, collisions play an important role and kinetic effects, such as trapping, are less important. The fluctuations and the background profiles have comparable amplitude and characteristic lengths, leading to meso-scale structures. Consequently, turbulence simulations addressing the scrape-off layer must be global and source driven. Finally, since scrape-off layer turbulence is dominated by ballooning modes driven by unfavorable curvature,[18,21,26,27] most of the relevant physics

can be captured with a cold ion fluid model. It is noted that adding an ion temperature equation (a) would increase the strength of the curvature drive term and (b) gives rise to the ion temperature gradient mode, which we expect to be stable at the parameter regime studied. These effects have been described in Ref. 28 in flux-tube geometry.

Starting from the Braginskii fluid equations,[29] we adopt the orderings $d/dt \ll \omega_{ci}$ ($\omega_{ci} = eB/m_i$ is the ion gyrofrequency), $k_\perp \gg k_\parallel$, and $T_i \ll T_e$, which lead, in normalized units, to the following drift-reduced equations:

$$\partial_t n = - R[\phi, n] - \nabla_\parallel(nv_{\parallel e}) + 2[\hat{C}(p_e) - n\hat{C}(\phi)] + S_n + D_n\nabla_\perp^2 n, \tag{1}$$

$$\partial_t \omega = - R[\phi, \omega] - v_{\parallel i}\nabla_\parallel \omega + \frac{2}{n}\hat{C}(p_e) + \frac{1}{n}\nabla_\parallel j_\parallel + \frac{1}{3n}\hat{C}(G_i) + D_\omega \nabla_\perp^2 \omega, \tag{2}$$

$$\partial_t\left(v_{\parallel e} + \frac{m_i}{m_e}\frac{\beta_{e0}}{2}\right) = - R[\phi, v_{\parallel e}] - v_{\parallel e}\nabla_\parallel v_{\parallel e} + D_{v_{\parallel e}}\nabla_\perp^2 v_{\parallel e} + \frac{m_i}{m_e}\left\{\nu\frac{j_\parallel}{n} + \nabla_\parallel\phi - \frac{1}{n}\nabla_\parallel p_e - 0.71 n\nabla_\parallel T_e - \frac{2}{3n}\nabla_\parallel G_e\right\}, \tag{3}$$

$$\partial_t v_{\parallel i} = - R[\phi, v_{\parallel i}] - v_{\parallel i}\nabla_\parallel v_{\parallel i} - \frac{1}{n}\nabla_\parallel p_e - \frac{2}{3n}\nabla_\parallel G_i + D_{v_{\parallel i}}\nabla_\perp^2 v_{\parallel i}, \tag{4}$$

$$\partial_t T_e = - R[\phi, T_e] - v_{\parallel e}\nabla_\parallel T_e + \frac{4}{3}T_e\left[\frac{7}{2}\hat{C}(T_e) + \frac{T_e}{n}\hat{C}(n) - \hat{C}(\phi)\right] + S_{T_e} + \frac{2}{3}T_e\left[0.71\nabla_\parallel v_{\parallel i} - 1.71\nabla_\parallel v_{\parallel e} + 0.71\left(\frac{v_{\parallel i} - v_{\parallel e}}{n}\right)\nabla_\parallel n\right] + D_{T_e}\nabla_\perp^2 T_e, \tag{5}$$

where $\omega = \nabla_\perp^2 \phi$ is the vorticity, $j_\parallel = n(v_{\parallel i} - v_{\parallel e})$ is the parallel current, and ν is the resistivity. The vorticity equation has been simplified using the Boussinesq approximation $\nabla \cdot (nd_t\nabla_\perp\phi) \approx nd_t\nabla_\perp^2\phi$. It is noted that, in recent 2D scrape-off layer simulations, it was found that the Boussinesq approximation does not change the turbulent dynamics significantly.[30] On the other hand, seeded blobs are faster and more stable when the Boussinesq approximation is relaxed.[31,32]

Plasma outflow from the closed flux surface region is mimicked using density and temperature sources, respectively, S_n and S_{T_e}. The G_e and G_i terms represent the gyroviscous part of the pressure tensor (see Ref. 22). Small perpendicular diffusion terms of the form $D_a\nabla_\perp^2 a$ are added for numerical reasons. In addition, $[a, b] = \hat{b}_0 \cdot [\nabla a \times \nabla b]$ is the Poisson bracket, while $\hat{C}(a) = (B/2)(\nabla \times (\hat{b}_0/B)) \cdot \nabla a$ is the curvature operator.

The Ohm's law (Eq. (3)) evolves the scalar function $v_{\parallel e} + m_i\beta_{e0}\psi/(2m_e)$, which represents a combination of ideal

induction and electron inertial effects. The scalar potential function $\beta_{e0}\psi/2 = -\hat{b}_0 \cdot \mathbf{A}_1$ is the parallel component of a vector potential function such that $\nabla \times \mathbf{A}_1 = \mathbf{B}_1$, and it is equal to the poloidal flux up to a constant. It can be shown that $\mathbf{B}_1 = -\nabla \times \beta_{e0}\psi\hat{b}_0/2$ is the perturbed perpendicular magnetic field, and that the perturbed and equilibrium magnetic field components are perpendicular to each other, $\mathbf{B}_1 \perp \mathbf{B}_0$. The parallel current and the poloidal flux function are related through Ampère's equation $\nabla_\perp^2\psi = j_\parallel$. Finally, the parallel gradient $\nabla_\parallel a = \hat{b}_0 \cdot \nabla a + \beta_{e0}R[\psi, a]/2$ takes into account the variation of scalar quantities along $\mathbf{B} = \mathbf{B}_0 + \mathbf{B}_1$.

The normalizations are (tilde denotes physical quantity in SI units): $t = \tilde{t}/(R/c_{s0})$, $\nabla_\perp = \tilde{\nabla}_\perp\rho_{s0}$, $\nabla_\parallel = \tilde{\nabla}_\parallel R$, $v = \tilde{v}/c_{s0}$, $n = \tilde{n}/n_0$, $T_e = \tilde{T}_e/T_{e0}$, $\phi = e\tilde{\phi}/T_{e0}$, $\psi = \tilde{\psi}/[2c_{s0}m_i/(e\beta_{e0})]$, $\nu = \tilde{\nu}/(c_{s0}/R)$, with $c_{s0} = \sqrt{T_{e0}/m_i}$ and $\rho_{s0} = c_{s0}/\omega_{ci}$, while T_{e0} and n_0 are the reference temperature and density and R is the tokamak major radius.

In the following, we concentrate on a scrape-off layer model with finite connection length and where the Shafranov shift is neglected. We leave the study of the second stability regime,[4] which appears when the Shafranov shift is included, for future studies. We adopt the $\hat{s} - \alpha$ circular geometry with a toroidal limiter set at the high field side equatorial mid-plane. Under these assumptions, the curvature operator reduces to $\hat{C}(a) = \sin\theta\partial_x a + (\cos\theta + \hat{s}\theta\sin\theta)\partial_y a$ and the Poisson bracket is defined as $[a, b] = \partial_y a\partial_x b - \partial_x a\partial_y b$. The coordinate system (y, x, z) is right handed; y is the poloidal angle multiplied by the minor radius, x is the radial coordinate, and z is the toroidal angle.

A set of boundary conditions appropriate for fluid simulations of the scrape-off layer was derived in Ref. 23 and is used in the non-linear simulations. They describe the interface between the scrape-off layer and the magnetic pre-sheath where the ion drift approximation $d/dt \ll \omega_{ci}$ breaks down. The boundary conditions used are as follows:

$$v_{\parallel i} = \pm c_s, \tag{6}$$

$$v_{\parallel e} = \pm c_s \exp(\Lambda - \phi/T_e), \tag{7}$$

$$\psi = 0, \tag{8}$$

$$\omega = -\cos^2\frac{r}{qR}\left[\left(\frac{\partial v_{\parallel i}}{\partial y}\right)^2 + c_s\frac{\partial^2 v_{\parallel i}}{\partial y^2}\right] \tag{9}$$

$$\frac{\partial n}{\partial y} = \pm\frac{n}{c_s}\frac{\partial v_{\parallel i}}{\partial y}, \tag{10}$$

$$\frac{\partial \phi}{\partial y} = \pm c_s\frac{\partial v_{\parallel i}}{\partial y}, \tag{11}$$

$$\frac{\partial T_e}{\partial y} = 0, \tag{12}$$

where $\Lambda \approx 3$. These quantities are evaluated at the top and bottom ends of the vertical domain. With respect to Ref. 23, corrections of order $\sim\rho_{s0}/L_p$ have been neglected and we have introduced the boundary condition for the poloidal flux.

Equations (1)–(5), together with the boundary conditions (Eqs. (6)–(12)), constitute the model that we use throughout the paper to study electromagnetic scrape-off layer turbulence.

III. LINEAR IDEAL STABILITY IN THE SCRAPE-OFF LAYER

Herein, we address ideal ballooning mode stability in a limited scrape-off layer configuration. The drift-reduced Braginskii model (Eqs. (1)–(5)) is a superset of the reduced MHD model, and therefore, it is appropriate to study ideal ballooning stability. The simplest model describing ideal ballooning stability can be obtained, starting from Eqs. (1)–(5), by ignoring collisions, gyroviscosities, ion parallel velocity, electron inertia, and Braginskii's thermal frictional force. Furthermore, compressibilities in the density and temperature equations, as well as parallel gradients of density and temperature in the Ohm's law are neglected. The diamagnetic terms in the Ohm's law are stabilizing. These and other two-fluid effects, which can affect the marginal stability threshold, are discussed in Ref. 5.

After taking these approximations, the density and temperature equations can be added to obtain an equation for pressure, and using the curvature operator $\hat{C}$ described in the Sec. II, we obtain the reduced MHD equations

$$\frac{\partial p}{\partial t} = -R[\phi, p], \tag{13}$$

$$\frac{\partial}{\partial t}\nabla_\perp^2\phi = 2\hat{C}(p) + \nabla_\parallel j_\parallel, \tag{14}$$

$$\frac{\beta_e}{2}\frac{\partial\psi}{\partial t} = \nabla_\parallel\phi. \tag{15}$$

Linearizing Eqs. (13)–(15), using Ampère's equation $\nabla_\perp^2\psi = j_\parallel$, and solving for the perturbed electrostatic potential ϕ_1, the following Sturm-Liouville problem is obtained:[2,3]

$$\frac{\partial}{\partial\theta}\left\{[1 + (\hat{s}\theta)^2]\frac{\partial\phi_1}{\partial\theta}\right\}$$
$$-\alpha\{\hat{\gamma}^2[1 + (\hat{s}\theta)^2] - (\cos\theta + \hat{s}\theta\sin\theta)\}\phi_1 = 0. \tag{16}$$

Here, $\hat{\gamma} = \gamma/\gamma_I$ is the growth rate normalized to the reference interchange growth rate $\gamma_I = \sqrt{2R/L_p}$. The poloidal angle θ (equivalent to the standard ballooning angle) is a field line following coordinate that starts on one limiter plate, winds around the torus q times, and ends on the other limiter plate. The equatorial mid-plane of the low-field side of the torus is set to $\theta = 0$, and therefore $-\pi \leq \theta \leq \pi$.

It is remarked that the finite length of the magnetic field lines in the scrape-off layer must be taken into account by restricting the domain to one connection length $L_\theta = 2\pi$ and by imposing appropriate boundary conditions at the field line ends. Linear boundary conditions can play an important role in the linear stability of an open field line region.[33–36]

Our linearized boundary conditions are motivated by the properties of the non-linear stage turbulence in the non-linear simulations. In the high β regime, where ideal ballooning modes are unstable, we have found that the potential

fluctuations are (a) strongly peaked in the bad curvature region and (b) small and roughly constant near the limiter in the good curvature region. In addition, it appears that the fluctuations decay strongly near the edge of the domain, with a characteristic decay length of roughly $5 - 10\rho_{s0}$. The small amplitude of the fluctuations at the domain edges is consistent with the typical case of a tokamak geometry where the limiter or divertor is far from the bad curvature region. We have chosen the simplest set of boundary conditions that capture these properties, i.e., $\phi_1(\theta = \pm\pi) = 0$. The method for numerical solution of Eq. (16) and a comparison with well known results are detailed in Appendix.

The linear stability of the system can be assessed by obtaining the largest real eigenvalue of Eq. (16). The results of our linear stability analysis are shown in Fig. 1, where we plot ideal ballooning mode growth rates $\hat{\gamma}$ as a function of the magnetic shear $\hat{s}$ and the ideal stability parameter α. A finite threshold $\alpha_{\text{crit}} \gtrsim 0.5$, which increases with $|\hat{s}|$, can be observed. On the other hand, if the connection length is increased or if Von Neumann boundaries are used, ideal ballooning modes can be unstable essentially at $\beta = 0$, and the stabilization with magnetic shear is not as pronounced (see Appendix). In essence, the short connection length $L_\theta = 2\pi$ and the Dirichlet boundary conditions are stabilizing because they impose a sharp decay length on the perturbation as it approaches the wall, limiting its growth over time.

IV. IDEAL BALLOONING MODES IN THE DRIFT-REDUCED BRAGINSKII MODEL

We now consider the onset of ideal ballooning modes in the full reduced Braginskii model. Braginskii's Ohm's law introduces resistivity, electron inertia, and diamagnetic flows. As a result, ballooning modes due to resistivity or inertial effects can become unstable.[37] The reduced Braginskii model also contains drift waves, which become the dominant linear electrostatic instability at low collisionality or large pressure gradient.[38] Interchange-like modes are dominant at high collisionality and weak pressure gradient where the inaccessible operating regime[10,11] is observed. Therefore,
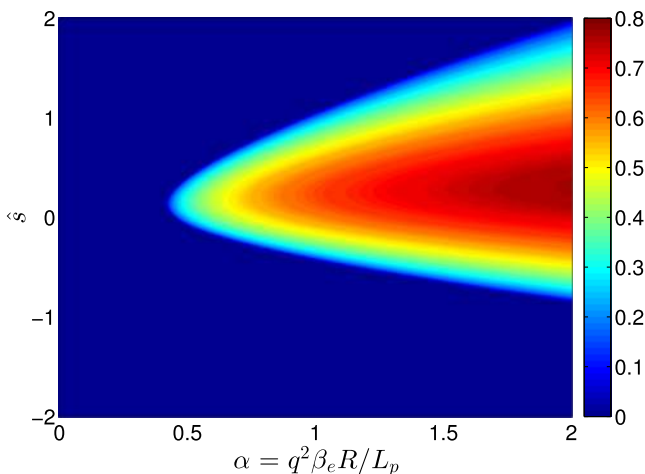

FIG. 1. Ideal ballooning mode growth rate $\hat{\gamma} = \gamma/\gamma_I$ is plotted as a function of $\hat{s}$ and $\alpha = q^2\beta_e R/L_p$. The growth rate is obtained from the largest real eigenvalue of Eq. (16) using Dirichlet boundary conditions, $L_\theta = 2\pi$.

the appearance of ideal ballooning modes is of particular interest in this regime, and our work concentrates on the transition between resistive and ideal ballooning modes.

A linear study has been carried out using the flux tube linear code described in Ref. 38, which implements a linearized version of Eqs. (1)–(5). The code solves for the perturbed quantities $[n_1, \phi_1, \psi_1, v_{\|i,1}, T_{e1}]$, which are discretized as a function of the standard ballooning angle θ in a finite domain of length $L_\theta = 2\pi$. The system of equations is advanced in time semi-implicitly and the growth rate is obtained from the ratio of the norm of the perturbed density over a long time period $\Delta t \gg \gamma^{-1}$.

We have chosen a simple set of linearized boundary conditions that is an extension of the conditions used in Sec. IV. The boundary conditions are $\phi_1(\theta = \pm\pi) = n_1(\theta = \pm\pi) = T_{e1}(\theta = \pm\pi) = 0$, while $\partial_\theta v_{\|i1} = \partial_\theta \psi_1 = 0$. It is noted that the boundary conditions chosen satisfy the structure of the linear equations automatically.

Using fixed $q = 6$, $\hat{s} = 0$, $\nu = 0.01$, $m_i/m_e = 200$, $L_y = 800$, $R = 500$, $L_p = 70, 40$, we scan over α by varying β_e and we consider the poloidal wave numbers $k_y \approx 0.05 - 0.95$ (toroidal mode numbers $n = 1 - 20$). The ideal MHD threshold is expected to be $\alpha_{\text{crit}} \approx 0.5$, as seen in Fig. 1. These parameters are representative of the non-linear steady-state simulations discussed in Sec. V. The linear growth rates are shown in Fig. 2. Similar trends are observed for both values of L_p. In the electrostatic regime $\alpha \ll 1$ resistive ballooning modes are the dominant unstable modes, damped at lower k_y by $k_\perp/k_\|$ effects.[38] This effect can be obtained, for instance, by considering a reduced model such as Eqs. (13) and (14) together with the Ohm's law $\nabla_\| \phi = \nu j_\|$ and taking $\hat{C}(p) \sim \partial_y p$ in the vorticity equation. The linear dispersion relation is, then, $\gamma^2 = \gamma_I^2 - \gamma k_\|^2/(k_\perp^2 \nu)$, meaning that, to be unstable, the mode must overcome a critical pressure gradient that increases with $k_\|$. It is observed, however, that this damping effect becomes weaker with increasing α, allowing longer wavelength modes to grow below the ideal ballooning threshold.

The destabilization of long wavelength resistive ballooning modes can be explained as follows. Consider Eqs. (13) and (14) together with the Ohm's law $(\beta_e/2)\partial_t \psi = \nu j_\| + \nabla_\| \phi$. Neglecting again the poloidal variation of the interchange drive term in the vorticity equation, it can be shown that the dispersion relation obtained from this system is

$$-\gamma^2\left(\nu + \frac{\beta_e}{2}\frac{\gamma}{k_\perp^2}\right) = -2\frac{R}{L_p}\left(\nu + \frac{\beta_e}{2}\frac{\gamma}{k_\perp^2}\right) + \frac{k_\|^2}{k_\perp^2}\gamma, \quad (17)$$

where the factor $(\beta_e/2)(\gamma/k_\perp^2)$ arises from the ideal induction term in the Ohm's law, and we have approximated $k_y = k_\perp$. The cubic term $\sim \beta_e \gamma^3$ on the left hand side of Eq. (17) represents the ideal ballooning branch; in the limit where $\alpha < \alpha_{\text{crit}}$ and $\gamma \ll 1$ it can be neglected. The induction term on the right hand side of the equation counteracts the parallel damping term, leading to the following dispersion relation for the resistive branch at marginal stability:

$$\gamma^2 \approx \gamma_I^2 - \gamma(1-\alpha)\frac{k_\|^2}{k_\perp^2 \nu}. \quad (18)$$

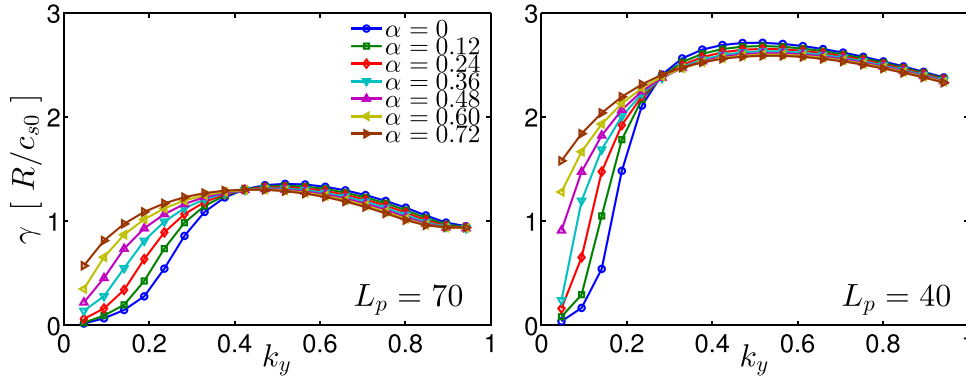FIG. 2. Linear growth rates obtained from Eqs. (1)–(5) for $k_y = 0.05$–0.95 (toroidal mode numbers $n < 20$). Low n modes become unstable as α increases.

It is concluded that finite β effects can allow the resistive ballooning branch to become unstable at lower perpendicular wavelengths than in the purely electrostatic case ($\alpha = 0$) as observed in Fig. 2 and also in Fig. 3.

Since ideal ballooning modes are expected to assume the smallest possible wavelength in the system, we have chosen to describe their onset as a function of α for $k_y = 0.05$, as shown in Fig. 3. The linear growth rates arising from several models are included for comparison: (a) complete reduced Braginskii model, (b) reduced Braginskii, without magnetic flutter terms in Ohm's law, (c) reduced Braginskii without induction term on the left hand side of Ohm's law, (d) ideal MHD, and (e) ideal MHD with magnetic flutter. The magnetic flutter terms in Eq. (3), which arise due to the parallel variation of density and temperature, are stabilizing for both the resistive and ideal branches (compare (a) with (b) and (e) with (d), respectively). The induction term is destabilizing for the resistive branch (compare (a) with (c) below the ideal threshold). In addition, it has been verified that the parallel convection and thermal force terms in the density and temperature equations are stabilizing. Finally, we note the inductive coupling between resistive and ideal ballooning modes by comparing (a) with (e). We therefore confirm that global modes can become unstable at $\alpha \lesssim \alpha_{\text{crit}}$ due to the inductive destabilization effect. These modes become stronger at the onset of the ideal ballooning mode $\alpha \gtrsim \alpha_{\text{crit}} \approx 0.5$.
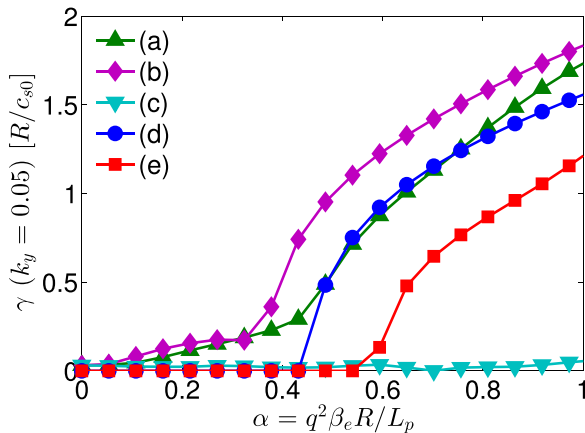

FIG. 3. Growth rate obtained from Eqs. (1)–(5) linearized in the following limits: (a) complete model, (b) complete model without magnetic flutter terms, (c) complete model without induction term, (d) ideal MHD model, and (e) ideal MHD with magnetic flutter terms.

V. NON-LINEAR SIMULATIONS AND IDEAL BALLOONING THRESHOLD

In this section, we describe non-linear 3D electromagnetic simulations of scrape-off layer turbulence carried out with GBS,[22] an initial value, global 3D non-linear code which advances in time the five scalar fields in Eqs. (1)–(5). GBS simulation results have been fully validated against experimental measurements from the TORPEX device.[39–41] The method of solution involves approximating the right hand side of the equations (i.e., the spatial derivatives) using standard second order accurate finite differences in space and the Arakawa scheme[42] for the Poisson brackets, while the time advance is carried out using fourth order Runge-Kutta integration. The boundary conditions, which control the plasma outflow into the limiter plates, are treated following the model presented in Ref. 23 and summarized in Eqs. (6)–(12).

The simulations are initialized using smooth profiles upon which a small perturbation is superimposed. The simulated scrape-off layer plasma undergoes first a transient phase, in which interchange modes become linearly unstable, driving turbulence that causes perpendicular transport. Over a longer time period, the turbulence saturates and a non-linear steady-state is achieved as a balance between the n and T_e sources mimicking the outflow from the core, turbulent transport, and parallel losses at the toroidal limiter. The pressure gradient length L_p, rather than being preset as in the linear calculations, is obtained self-consistently from the balance between plasma sources, turbulent transport, and parallel losses.

The following numerical parameters were used for the simulations: $n_x = 128, n_y = 768, n_z = 64$ (n_x, n_y, and n_z are the number of radial, poloidal, and toroidal grid points, respectively). This grid results in a maximum poloidal wave number $k_{y,\text{max}} = 3$, while the largest unaliased toroidal mode number, applying the two-thirds rule, is $n_{\text{max}} = 21$. The physical parameters considered for the simulations are $q = 6, \hat{s} = 0, L_x = 100, L_y = 800, R = 500, \nu = 0.01 c_{s0}/R$, $m_i/m_e = 200$. The source terms S_n and S_{T_e} in Eqs. (1) and (5) have the form $S = S_0 \exp[-(x - x_S)^2/\sigma_S^2]$, with $S_0 = 1$, $x_S = 30$, and a characteristic width $\sigma_s = 5$. These source terms mimic the outflow of plasma from the closed flux surface region, and, therefore, the simulations are physically meaningful for $x > x_S$. For simplicity, they are taken to be constant in y and independent of n and T_e. In previous work,[25] the source strength was varied by a factor of four

without significant changes in the dynamics. In the absence of turbulence, the source terms would reach a balance with the parallel losses.

As the strength of the electromagnetic terms scales with the reference β_{e0} value, we carry out a scan with $\beta_{e0} = 10^{-4}, 2 \times 10^{-4}, 5 \times 10^{-4}, 7 \times 10^{-4}, 10^{-3}, 3 \times 10^{-3}$. In the Tokamak à Configuration Variable,[43] for example, $\beta \sim 10^{-5}$ is typical in the scrape-off layer.[26] It is remarked that electromagnetic effects enter the equations through the left hand side of the Ohm's law (Eq. (3)) and through the magnetic flutter terms in the parallel gradients, while only the magnetic flutter terms in the Ohm's law and in the ion parallel velocity equations enter the equations linearly.

Low frequency, collisional, interchange-like turbulent modes are recovered in the non-linear regime. Our analysis concentrates on the normalized pressure gradient L_p, the toroidal mode number n, the vertical wave number k_y, and the radial length of the turbulent structures. Principally, three changes in the character of the turbulence are observed as β_{e0} is increased: (a) L_p increases, (b) n and k_y decrease, and (c) the turbulent eddy radial extension increases.

As an example, poloidal cross sections of the plasma pressure are shown in Fig. 4 for simulations with $\beta_{e0} = 10^{-4}$ (left, similar to a purely electrostatic case), $\beta_{e0} = 10^{-3}$ (center, near the linear ideal threshold), and $\beta_{e0} = 3 \times 10^{-3}$ (right, ideal unstable). The characteristic lengths of the pressure profiles are superimposed as dashed lines, which represent L_p on the bad curvature side.

As a matter of fact, the obtained plasma profiles decay exponentially as a function of radius with a characteristic
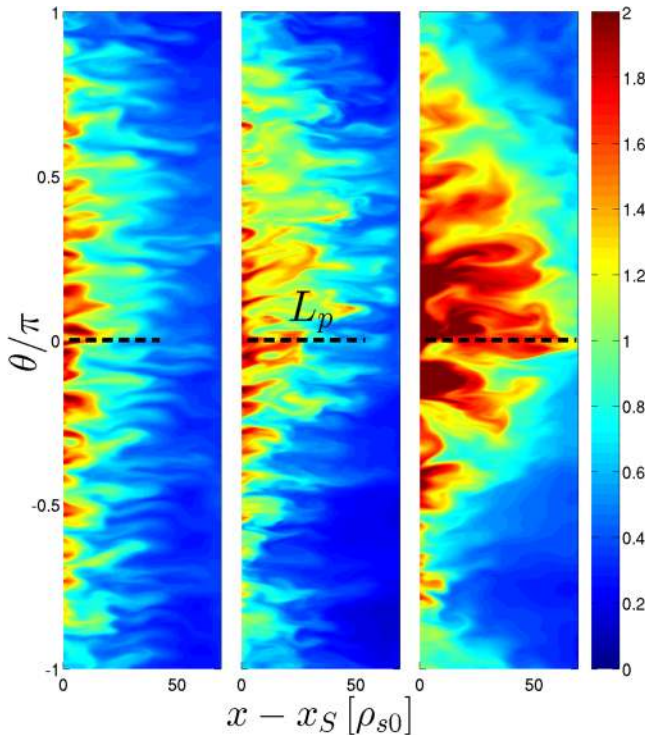

FIG. 4. Poloidal cross-sections of plasma pressure during the non-linear stage of GBS simulations are plotted for simulations with (left to right) $\beta_e = 10^{-4}, 10^{-3}, 3 \times 10^{-3}$ while the ideal stability parameter for each case is $\alpha = 0.06, 0.35, 0.89$. The dashed lines mark the profile length L_p.

length $L_p \sim -\nabla p / p$, such that $p \sim \exp(-x/L_p)$ with L_p increasing as a function of β_{e0}. For the cases with $\beta_{e0} = 10^{-4}, 10^{-3}, 3 \times 10^{-3}$ we have found, respectively, $L_p \approx 40, 53, 70$ and, consequently, $\alpha = 0.06, 0.35, 0.89$. The case with $\beta_{e0} = 3 \times 10^{-3}$ resides above α_{crit}—it is dominated by ideal ballooning modes that assume the lowest possible k_y available in the system. As expected, transport increases and the pressure gradient decreases significantly as the ideal threshold is approached and surpassed. This transition to globality is also illustrated in Fig. 5, which shows a radial cross section of the non-linear turbulent states; the dominant toroidal mode number decreases while the pressure length increases. As an aside, we note that poloidal asymmetry around $\theta = 0$ is sometimes observed in the plasma equilibrium profiles. This asymmetry is caused by the mean $\mathbf{E} \times \mathbf{B}$ bulk poloidal flow.

The non-linear turbulent spectrum is dominated by fluctuations with $n \lesssim 10$ and $k_y \sim 0.1$. The dominant k_y and the dominant toroidal number n visibly decrease as β_{e0} increases. This effect is shown in Fig. 6, where the power spectrum of the pressure fluctuations is plotted as a function of the poloidal wave number k_y (left) and toroidal mode number n (right). It is observed that the fluctuations gradually shift to a lower k_y and to a lower n as β_{e0} is increased. In the quasi-electrostatic regime the fluctuation spectrum is broad at low frequency, peaking roughly at $k_y \approx 0.15$ and then decaying rapidly. Local maxima occur at about every six wave numbers, and they correspond to field aligned modes with $m = nq$. At the highest value of β_{e0}, the dominant mode has $k_y \approx 0.05$, which corresponds to the $n = 1$ field aligned mode. Modes with $n > 1$ have a significantly lower amplitude, as observed directly from the right panels of Figs. 4 and 5. We note that in the low β_{e0} quasi-electrostatic regime, the fastest growing linear mode has $k_y \approx 0.5$, while in the high β_{e0} regime ideal ballooning modes grow at the shortest wavelength allowed by the system.

The shift in n and k_y takes place incrementally with β_{e0}, rather than abruptly, and it is accompanied by an increase in the radial length of the eddies, σ_x. As a way of quantifying the radial extent of the typical turbulent structure, we have evaluated the eddy radial extension of the perturbed density, perturbed electrostatic potential, and perturbed $\mathbf{E} \times \mathbf{B}$ turbulent particle flux $\Gamma_n = R\langle n_1 \partial_y \phi_1 \rangle$ as follows. First, we compute the self-correlation function, which for a quantity a is defined as $C(x_0, dx, dt) = \langle a(x_0 + dx, t + dt)a(x_0, t)\rangle_t / \langle a(x_0, t)a(x_0, t)\rangle_t$. The eddy length σ_x is the x-width of the $C = 0.5$ contour in the (dx, dt) plane. It has been verified that the σ_x obtained are robust with respect to the choice of x_0, for $x_S \lesssim x_0 \lesssim x_S + L_p$. The results are shown in Fig. 7, where the σ_x is plotted as a function of β_{e0}. The correlation lengths of the electrostatic potential and Γ_n are doubled from the lowest to the highest β_{e0}, while the increase is less marked for the density. The density correlation length appears to be roughly constant below $\beta_{e0} \approx 10^{-3}$. Similar trends were observed in Ref. 44.

From these results, it can be inferred that scrape-off layer turbulence is moderately affected by finite beta effects until a pressure threshold is reached. Predictably, longer wavelengths and larger correlation lengths lead to flatter profiles near the ideal threshold. In Sec. VI, we analyze these
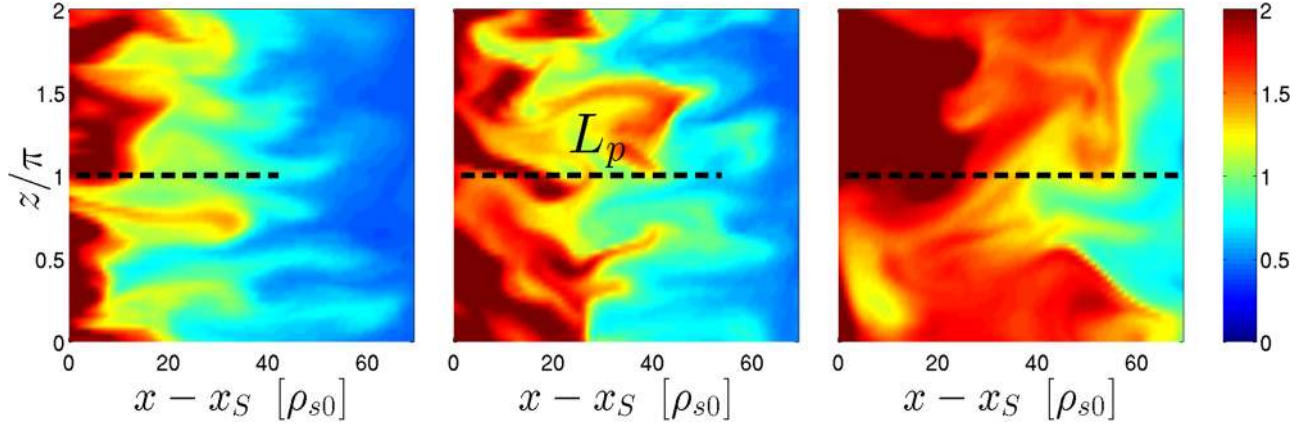
FIG. 5. Radial cross-sections of plasma pressure during the non-linear stage of GBS simulations are plotted for simulations with (left to right) $\beta_e = 10^{-4}$, 10^{-3}, 3×10^{-3} while the ideal stability parameter for each case is $\alpha = 0.06$, 0.35, 0.89. The radial cut is carried out at the equatorial midplane.
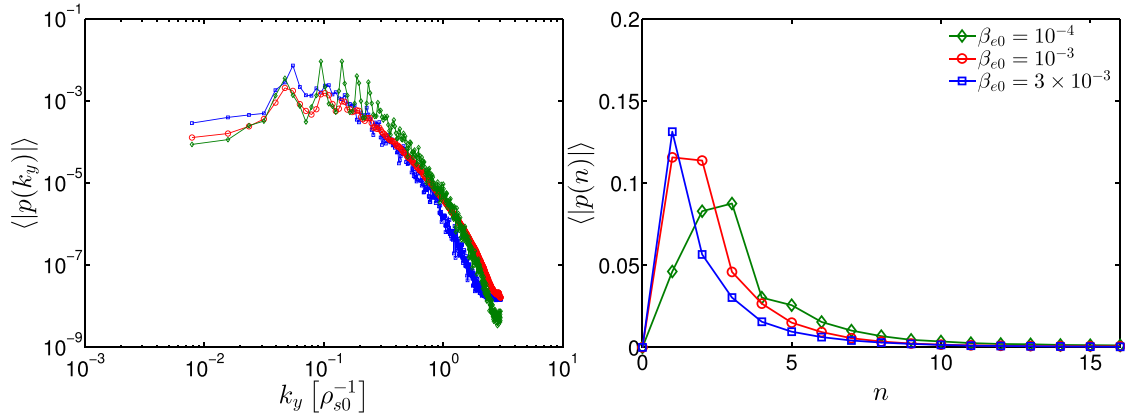

FIG. 6. Power spectrum of pressure fluctuations during the non-linear stage of GBS simulations are plotted as a function of poloidal wave number k_y (left) and toroidal mode number n (right). The simulations have $\beta_{e0} = 10^{-4}$, 10^{-3}, 3×10^{-3} (diamonds, circles, and squares, respectively).

phenomena in the framework of the saturation mechanism described in Refs. 24 and 25.

VI. TURBULENT SPECTRUM, SATURATION, AND ELECTROMAGNETIC EFFECTS

Some characteristics of the non-linear turbulent regime appear to be well-described by the *gradient removal*
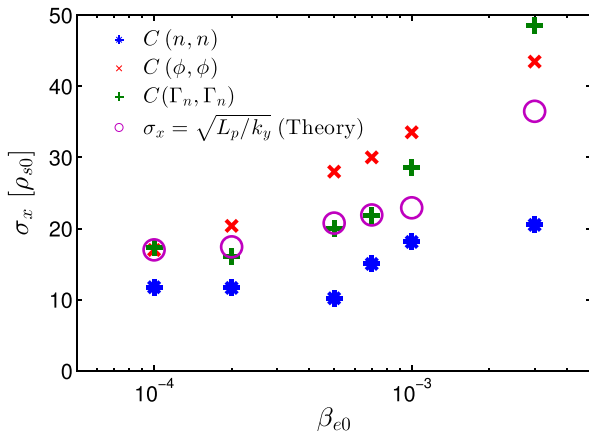

FIG. 7. Radial correlation lengths of n ($*$), ϕ ($\times$), and electrostatic $\mathbf{E} \times \mathbf{B}$ particle flux Γ_n ($+$) are plotted as a function of β_{e0}. Radial length of electrostatic potential eddies $\sigma_x = \sqrt{L_p/k_y}$ ($\circ$), estimated from a non-local linear theory, is shown for comparison.

mechanism.[24,25] The main features of this model are summarized as follows. We hypothesize that in the scrape-off layer instabilities can grow until they exhaust the linear drive provided by background profiles, which leads to the saturation condition $p_1/p_0 \sim \sigma_x/L_p$ (p_0 is the background pressure). This behavior, for example, was observed in non-linear turbulence simulations of interchange modes in a simple magnetized torus configuration,[24,45] resistive ballooning modes in the tokamak scrape-off layer,[25] and also ideal ballooning modes in the tokamak edge.[9] We remark that the GBS code is ideally suited to study the gradient removal mechanism because there is no separation between fluctuations and background, and therefore the saturation level is attained self-consistently.

The radial turbulent $\mathbf{E} \times \mathbf{B}$ flux $\Gamma = R\langle p_1 \partial_y \phi_1 \rangle$ can now be estimated if the characteristic radial length of the mode, σ_x, and the radial $\mathbf{E} \times \mathbf{B}$ velocity are known. An analysis carried out using a linear non-local theory[24,45,46] yields $\sigma_x \approx \sqrt{L_p/k_y}$, while the perturbed $\mathbf{E} \times \mathbf{B}$ velocity is estimated from the leading order terms of $\partial_t p = -R[\phi, p]$, which yields $\partial_y \phi_1 R/L_p \sim \gamma p_1/p_0$. The radial flux driven by the turbulent modes can, therefore, be approximated as

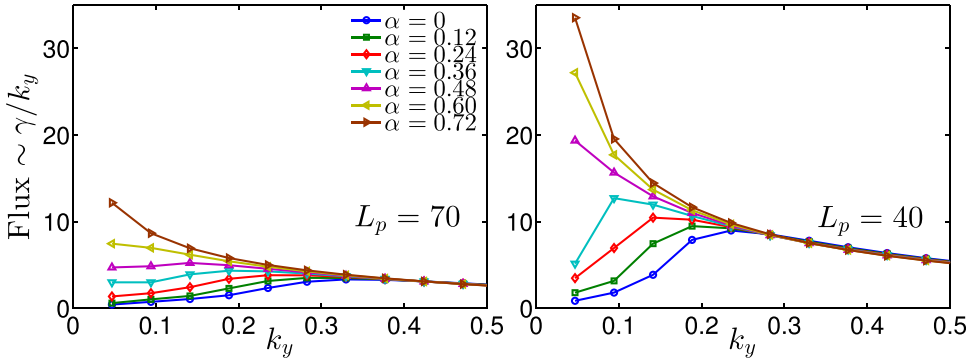$$\Gamma \sim p_0 \left(\frac{\gamma}{k_y} \right)_{\text{max}}, \tag{19}$$

FIG. 8. Estimated flux $\Gamma \sim \gamma/k_y$ obtained from linear reduced Braginskii model together with the gradient removal saturation rule (Eq. (19)). The normalized pressure gradients are $R/L_p = 7.15$ (left) and 12.5 (right). A shift to lower wave number k_y is observed as α increases.

where $(\gamma/k_y)_{\text{max}}$ represents one single poloidal mode that maximizes the turbulent flux. As a consequence, transport should increase with increasing linear drive and with small k_y. In the non-linear steady-state, the divergence of the radial turbulent flux, Γ/L_p, should be approximately balanced by the parallel losses $\nabla_{\|}p_0 v_{\|e} \approx p_0 c_s/q$, which leads to a scaling for the pressure profile radial decay length

$$\frac{L_p}{q} \sim \left(\frac{\gamma}{k_y}\right)_{\text{max}}. \tag{20}$$

In order to illustrate the expected level of transport as β_e is increased, the gradient removal mechanism is applied to the linear growth rates shown in Fig. 2. The flux predicted using Eq. (19) for that set of parameters is shown in Fig. 8. We consider $L_p = 70$ and $L_p = 40$, which are obtained, respectively, in non-linear simulations with $\beta_{e0} = 3 \times 10^{-3}$ and $\beta_{e0} = 10^{-4}$. In the electrostatic regime, α is very low and we expect the non-linear steady-state regime to be dominated by a mode with $k_y \sim 0.2$. As α is increased, it is found that the maximum of γ/k_y shifts to lower k_y even below $\alpha_{\text{crit}} \approx 0.5$. A global instability with $n = 1$ is found to dominate the flux for $\alpha \gtrsim 0.5$.

In the non-linear simulations, L_p, k_y, the perpendicular flux, and the parallel losses all change self-consistently as β increases. First, as shown in Fig. 7, the estimate of the radial scale length of the mode, $\sigma_x \approx \sqrt{L_p/k_y}$, matches reasonably well the correlation length of the potential fluctuations as a function of β_{e0}, with $15 \lesssim \sigma_x \lesssim 35$. Furthermore, the profile

FIG. 9. Scaling of the pressure profile decay length $L_p \sim q(\gamma/k_y)_{\text{max}}$ obtained as a function of β_{e0} from Eq. (20).

lengths and the flux scaling predicted by Eq. (20) can be computed with the aid of the linear code used in Sec. IV. The calculation is carried out by obtaining $(\gamma/k_y)_{\text{max}}$ as a function of L_p until $(\gamma/k_y)_{\text{max}} = L_p/q$ for each desired value of β_{e0}. Note that the L_p and k_y from the gradient removal theory are therefore found self-consistently from Eq. (20). Figure 9 shows the gradient removal-estimated pressure scale length obtained from the balance of perpendicular to parallel losses, compared to the L_p obtained from GBS simulations. The trend recovered is that the pressure gradient is more or less constant until a critical β_{e0} threshold is reached. In the non-linear simulations, the parallel loss term $\nabla_{\|}(p v_{\|e})$ becomes greater at high β_{e0} due to poloidal peaking of the equilibrium profiles. We have evaluated Eq. (20) estimating $\nabla_{\|}(p v_{\|e})$ from the non-linear simulations—the results from Fig. 9 were not significantly altered.

VII. CONCLUSIONS

In the present work, we have investigated electromagnetic effects in turbulent plasmas in the tokamak scrape-off layer, concentrating on the transition between resistive and ideal ballooning modes. Our main findings can be summarized as follows. Linearly, it was found that resistive ballooning modes are enhanced by an induction effect when beta is increased, while ideal ballooning modes become destabilized at the threshold expected from the MHD theory. We have also verified that, in the non-linear stage, the turbulence level is set by the gradient removal mechanism, the non-linear local flattening of the pressure profile. It is also remarked that even the linear stability of long wavelength modes dominant in the scrape-off layer is strongly affected by the boundary conditions. Therefore, the study of turbulent dynamics in the scrape-off layer requires a full flux surface treatment and an accurate description of the plasma conditions at the magnetic pre-sheath entrance. More details summarizing our work, step by step, follow below.

First, it was found that the ideal stability boundary is affected by the boundary conditions imposed at the end of the field lines. Historically, periodicity played an important role in the development of ballooning theory, which manifests itself again here through the necessity to fulfill boundary conditions at the plasma wall interface and finite field line length. We chose to satisfy a "line-tied," Dirichlet boundary condition $\phi_1(\theta = \pm\pi) = 0$ as suggested by our non-linear results. This solution to the ballooning equation[2] yields a higher marginal stability limit than the standard
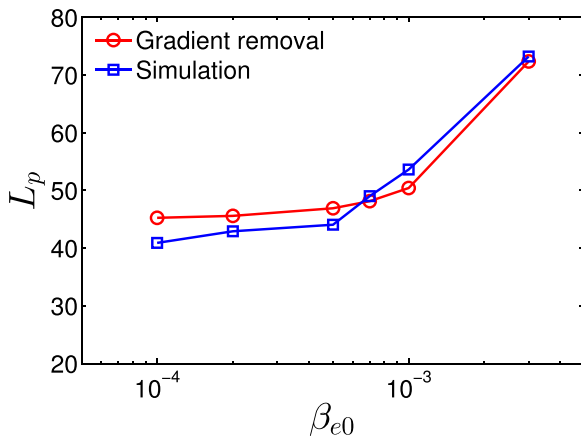
strongly ballooning solution, as first pointed out by Connor.[3] Section IV shows linear calculations that were carried out using a reduced MHD model. They show $\alpha_{crit} \approx 0.5$ at $\hat{s} = 0$ (see Fig. 1). We have carried out additional stability calculations, discussed in Appendix. Dirichlet boundary conditions are strongly stabilizing respect to Von Neumman boundary conditions ($\partial_\theta \phi(\theta = \pm\pi) = 0$).

The linear calculations have been extended to include collisions and two-fluid effects (Figs. 2 and 3). At low α, well below the ideal limit, we have found linearly unstable resistive ballooning modes with $\gamma_{max} \sim \sqrt{2R/L_p}$, peaking at moderate toroidal mode number n but also unstable at much longer wavelengths. As the plasma beta is increased, modes with increasingly longer wavelength are driven unstable by magnetic induction effects. The diamagnetic terms in Ohm's law are found to be stabilizing for the ideal branch, but their effect appears to be negated by the influence of the induction term on the resistive branch.

Flux-driven, global simulations were carried out in order to characterize the non-linear dynamics. The interface between the scrape-off layer plasma and the limiter plates at the vertical ends of the simulation domain, Eqs. (6)–(12), is consistent with a magnetic pre-sheath entrance condition.[23] The reference plasma β_{e0} was varied by a factor of 30. The simulations show profiles that are rather flat, with $L_p \approx 40 - 70$. In the low β_{e0} limit, we recover quasi-electrostatic, low-frequency, resistive ballooning turbulence. As β_{e0} is increased, a transition towards increased transport is observed, characterized by an increase of the profile lengths, a decrease of the perpendicular wavelengths, and an increase of the radial length of the turbulent eddies. Turbulence is gradually enhanced as α_{crit} is approached, and then strongly driven ideal ballooning modes are found. The "ideal limit" is interpreted as a transition to a global mode with $n = 1$.

The β scaling of L_p obtained in the non-linear simulations is in good agreement with the prediction of the gradient removal theory, $L_p = q(\gamma/k_y)_{max}$. Therefore, the transition towards globality observed in the simulations is interpreted as a gradual shift toward long wavelength modes excited by

an electromagnetic modification of the parallel dynamics. Then, a linearly unstable ideal mode can grow if $\alpha > \alpha_{crit}$, driving eddies with a radial length comparable to the radial simulation domain. The scaling of the flux and pressure gradient length, given by the gradient-removal theory and by the non-linear simulations, suggests a relatively modest and gradual influence of electromagnetic effects until a pressure threshold is reached.

APPENDIX: ANALYSIS OF THE STURM-LIOUVILLE PROBLEM FOR IDEAL BALLOONING MODES

While typically Eq. (16) is solved using a shooting code, we have chosen to write it as a standard eigenvalue problem of the form $\mathbf{A}(\phi_1) = \lambda\phi_1$. The left hand side of the equation is then discretized along a finite domain in θ using standard second order accurate centered finite differences. This procedure results in a tridiagonal system of algebraic equations of the form $\mathbf{A}_{ij}\phi_{1,j} = \lambda\phi_{1,j}$. The eigenvalues $\lambda_i = \alpha\hat{\gamma}_i^2$ and the eigenfunctions of this system are obtained directly using a standard MATLAB routine.

We observe that, if the system is unstable, only one of the eigenvalues has a positive real part. Additionally, the eigenmodes are either purely oscillating or purely growing, as required by the self-adjointness property of the ideal
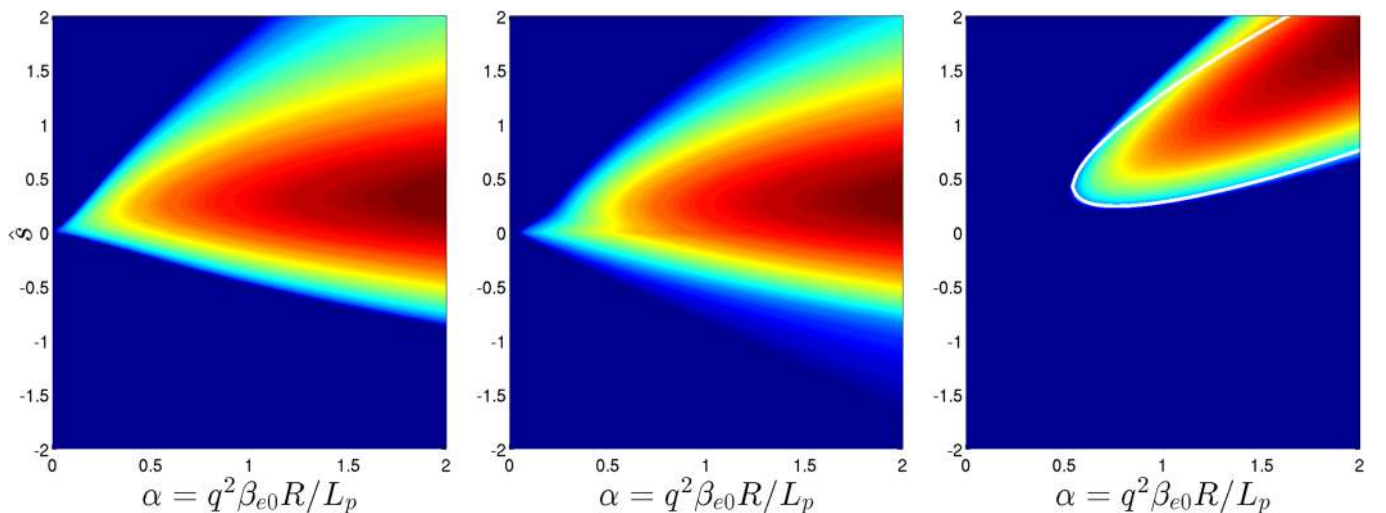

FIG. 10. Ideal ballooning mode growth rate $\hat{\gamma} = \gamma/\gamma_1$ is plotted as a function of $\hat{s}$ and $\alpha = q^2\beta_e R/L_p$. We show three different cases: $L_\theta = 2\pi$, $\partial_y\phi(\theta = \pm\pi) = 0$ (left); $L_\theta = 32\pi$, $\phi(\theta = \pm\pi) = 0$ (center); and (right, same case as Ref. 2, which includes Shafranov's shift) $L_\theta = 2\pi$, $\phi(\theta = \pm\pi) = 0$.

MHD force operator. Finally, it is noted that, within this numerical scheme, it is straightforward to choose between Dirichlet or Von Neumann boundary conditions.

In order to illustrate the importance of periodicity and boundary conditions, we have calculated ideal ballooning mode growth rates for the following cases: using the same parameters as in Fig. 1 but using Von Neumann boundary conditions $\partial_\theta \phi_1(\theta = \pm\pi) = 0$ (left panel of Fig. 10) and (b) the same as in Fig. 1 but with very large connection length $L_\theta = 32\pi$ (center panel of Fig. 10). The result is that, compared to Fig. 1, the marginal stability limit decreases significantly in both cases.

We also reproduce a well known result[2] to verify our numerical implementation. Here we include Shafranov's shift, which gives $\hat{C}(a) = k_y[\cos\theta + (\hat{s}\theta - \alpha\sin\theta)\sin\theta]a$. In his description of the ballooning mode topology, Coppi suggested a trial function $\phi = 1 + \cos\theta$ in the domain $-\pi < \theta < \pi$ and $\phi = 0$ otherwise. Curiously, this trial function satisfies a Dirichlet boundary condition $\phi(\theta = \pm\pi) = 0$, and it is therefore adequate for studying scrape-off layer stability. The growth rates obtained numerically from Eq. (16) are shown in on the right panel of Fig. 10. An analytical function for marginal stability can be obtained from the energy principle using Coppi's trial eigenfunction,[6] and it is shown as a white curve on the figure. The marginal stability from Refs. 3 and 4 has also been verified.

[1]F. Troyon, R. Gruber, H. Saurenmann, S. Semenzato, and S. Succi, Plasma Phys. Controlled Fusion **26**, 209 (1984).

[2]B. Coppi, Phys. Rev. Lett. **39**, 939 (1977).

[3]J. W. Connor, R. J. Hastie, and J. B. Taylor, Phys. Rev. Lett. **40**, 396 (1978).

[4]J. Greene and M. Chance, Nucl. Fusion **21**, 453 (1981).

[5]R. Hazeltine and J. Meiss, Phys. Rep. **121**, 1 (1985).

[6]J. P. Freidberg, *Ideal Magnetohydrodynamics* (Plenum Press, New York, 1987), Chap. 10, pp. 393–419.

[7]H. Lütjens and J.-F. Luciani, Phys. Plasmas **4**, 4192 (1997).

[8]B. N. Rogers, J. F. Drake, and A. Zeiler, Phys. Rev. Lett. **81**, 4396 (1998).

[9]B. D. Scott, Phys. Plasmas **12**, 062314 (2005).

[10]B. LaBombard, J. Hughes, D. Mossessian, M. Greenwald, B. Lipschultz, J. Terry, and the Alcator C-Mod Team, Nucl. Fusion **45**, 1658 (2005).

[11]B. LaBombard, J. W. Hughes, N. Smick, A. Graf, K. Marr, R. McDermott, M. Reinke, M. Greenwald, B. Lipschultz, J. L. Terry, D. G. Whyte, S. J. Zweben, and the Alcator C-Mod Team, Phys. Plasmas **15**, 056106 (2008).

[12]B. N. Rogers and J. F. Drake, Phys. Rev. Lett. **79**, 229 (1997).

[13]B. Scott, Plasma Phys. Controlled Fusion **39**, 471 (1997).

[14]V. Naulin, Phys. Plasmas **10**, 4016 (2003).

[15]B. Scott, Plasma Phys. Controlled Fusion **39**, 1635 (1997).

[16]Y. Sarazin, Ph. Ghendrih, G. Attuel, C. Clément, X. Garbet, V. Grandgirard, M. Ottaviani, S. Benkadda, P. Beyer, N. Bian, and C. Figarella, J. Nucl. Mater. **313**, 796 (2003).

[17]O. E. Garcia, J. Horacek, R. A. Pitts, A. H. Nielsen, W. Fundamenski, J. P. Graves, V. Naulin, and J. J. Rasmussen, Plasma Phys. Controlled Fusion **48**, L1 (2006).

[18]O. Garcia, J. Horacek, R. Pitts, A. Nielsen, W. Fundamenski, V. Naulin, and J. J. Rasmussen, Nucl. Fusion **47**, 667 (2007).

[19]S. J. Zweben, B. D. Scott, J. L. Terry, B. LaBombard, J. W. Hughes, and D. P. Stotler, Phys. Plasmas **16**, 082505 (2009).

[20]J. R. Myra, D. A. Russell, D. A. D'Ippolito, J.-W. Ahn, R. Maingi, R. J. Maqueda, D. P. Lundberg, D. P. Stotler, S. J. Zweben, J. Boedo, M. Umansky, and the NSTX team, Phys. Plasmas **18**, 012305 (2011).

[21]F. Militello, W. Fundamenski, V. Naulin, and A. H. Nielsen, Plasma Phys. Controlled Fusion **54**, 095011 (2012).

[22]P. Ricci, F. D. Halpern, S. Jolliet, J. Loizu, A. Mosetto, A. Fasoli, I. Furno, and C. Theiler, Plasma Phys. Controlled Fusion **54**, 124047 (2012).

[23]J. Loizu, P. Ricci, F. D. Halpern, and S. Jolliet, Phys. Plasmas **19**, 122307 (2012).

[24]P. Ricci, B. N. Rogers, and S. Brunner, Phys. Rev. Lett. **100**, 225002 (2008).

[25]P. Ricci and B. N. Rogers, Phys. Plasmas **20**, 010702 (2013).

[26]J. Horacek, "Measurement of edge electrostatic turbulence in the TCV tokamak plasma boundary," Ph.D. dissertation, No. 3524, École Polytechnique Fédérale de Lausanne, Lausanne (2006).

[27]T. T. Ribeiro and B. Scott, Plasma Phys. Controlled Fusion **50**, 055007 (2008).

[28]A. Zeiler, D. Biskamp, J. F. Drake, and B. N. Rogers, Phys. Plasmas **5**, 2654 (1998).

[29]S. I. Braginskii, *Transport Processes in a Plasma*, edited by M. A. Leontovich, *Reviews of Plasma Physics, Vol. 1* (Consultants Bureau, New York, 1965), p. 205.

[30]K. Bodi, G. Ciraolo, Ph. Ghendrih, F. Schwander, E. Serre, and P. Tamain, in *38th EPS Conference on Plasma Physics* (Strasbourg, France, 2011), P1.121.

[31]G. Q. Yu, S. I. Krasheninnikov, and P. N. Guzdar, Phys. Plasmas **13**, 042508 (2006).

[32]D. Russell, D. D'Ippolito, and J. Myra, Bull. Am. Phys. Soc. **57**, BP8.00159 (2012).

[33]S. V. Novakovskii, P. N. Guzdar, J. F. Drake, and C. S. Liu, Phys. Plasmas **2**, 3764 (1995).

[34]W. Kerner, A. Nassigh, and O. Pogutse, Plasma Phys. Controlled Fusion **39**, 1101 (1997).

[35]E. Hameiri, Phys. Plasmas **6**, 674 (1999).

[36]D. D. Ryutov, I. Furno, T. P. Intrator, S. Abbate, and T. Madziwa-Nussinov, Phys. Plasmas **13**, 032105 (2006).

[37]T. Rafiq, G. Bateman, A. H. Kritz, and A. Y. Pankin, Phys. Plasmas **17**, 082511 (2010).

[38]A. Mosetto, F. D. Halpern, S. Jolliet, and P. Ricci, Phys. Plasmas **19**, 112103 (2012).

[39]A. Fasoli, B. Labit, M. McGrath, S. H. Muller, G. Plyushchev, M. Podesta, and F. M. Poli, Phys. Plasmas **13**, 055902 (2006).

[40]P. Ricci, C. Theiler, A. Fasoli, I. Furno, B. Labit, S. H. Muller, M. Podesta, and F. M. Poli, Phys. Plasmas **16**, 055703 (2009).

[41]P. Ricci, C. Theiler, A. Fasoli, I. Furno, K. Gustafson, D. Iraji, and J. Loizu, Phys. Plasmas **18**, 032109 (2011).

[42]A. Arakawa, J. Comput. Phys. **1**, 119 (1966).

[43]S. Coda for the TCV Team, Nucl. Fusion **51**, 094017 (2011).

[44]S. Konzett, D. Reiser, and A. Kendl, Plasma Phys. Controlled Fusion **54**, 025011 (2012).

[45]P. Ricci and B. N. Rogers, Phys. Plasmas **16**, 062303 (2009).

[46]B. N. Rogers and W. Dorland, Phys. Plasmas **12**, 062511 (2005).